**PAPER • OPEN ACCESS**

# Near- and far scrape-off layer transport studies in detached, small-ELM ASDEX Upgrade discharges by means of EMC3-EIRENE

View the article online for updates and enhancements.

**IOP ebooks**™

Bringing together innovative digital publishing with leading authors from the global scientific community.

Start exploring the collection–download the first chapter of every title for free.

# Near- and far scrape-off layer transport studies in detached, small-ELM ASDEX Upgrade discharges by means of EMC3-EIRENE

**T Lunt**[1], **H Frerichs**[2], **M Bernert**[1], **D Brida**[1], **D Carralero**[3], **M Cavedon**[1], **P David**[1], **A Drenik**[1], **M Faitsch**[1], **Y Feng**[5], **M Griener**[1], **A Herrmann**[1], **B Kurzan**[1], **O Pan**[1,4], **U Plank**[1], **D Silvagni**[1,4], **M Willensdorfer**[1], **M Wischmeier**[1], **E Wolfrum**[1] and the ASDEX Upgrade team[6]

[1] Max Planck Institute for Plasma Physics, Boltzmannstr. 2, 85748 Garching, Germany

[2] University of Wisconsin, 1500 Engineering Drive, Madison, WI 53706, United States of America

[3] Ciemat, Av. Complutense, 40, 28040 Madrid, Spain

[4] Physik-Department E28, Technische Universität München, James-Franck-Str. 1, 85748 Garching, Germany

[5] Max Planck Institute for Plasma Physics, Wendelsteinstr. 1, 17491 Greifswald, Germany

E-mail: tilmann.lunt@ipp.mpg.de

## Abstract

We compare various diagnostics characterizing an ASDEX Upgrade upper single-null discharge to EMC3-EIRENE simulations now including volumetric recombination and main chamber plasma-wall interaction but not yet drifts. The discharge is in a small-ELM regime and is approaching detachment due to a density ramp and nitrogen seeding. Time/ELM averaged upstream density, electron and ion temperature measurements as well as downstream ion saturation current, electron temperature and power flux measurements match the simulation within the error bars before and after reaching detachment, qualifying the code for this regime. Although the Ion Cyclotron Resonance Heating (ICRH) antenna limiters are 35 mm away from the separatrix, i.e. ten times the typical near-SOL power fall-off length $\lambda_q^{near} = 3.8$ mm, they receive power fluxes of several hundreds of kW exceeding the ones to the outer target in the detached phase and strongly contribute to the particle fueling. This is explained by a substantially larger far-SOL power fall-off length $\lambda_q^{far} = 25$ mm possibly caused by the small ELMs in the detached phase and the occurrence of a density shoulder.

Keywords: power exhaust, detachment, ASDEX Upgrade, EMC3-EIRENE, Tokamak

(Some figures may appear in colour only in the online journal)

---

[6] see the author list [1]

## 1. Introduction & motivation

Due to the very short power fall-off length $\lambda_q$ in the scrape-off layer (SOL) of a divertor tokamak close to the separatrix [2], a large fraction of the power exhausted from the confinement region is deposited onto the small areas near the divertor strike points. While the power flux densities in these regions challenge the material limits already today, these

fluxes are expected to increase with machine size [3]. For this reason it is mandatory for ITER and DEMO to operate in the partially detached divertor regime, where power and particle fluxes near the strike points are substantially reduced [4]. Several authors [5–7] have reported the occurrence of an enhanced filamentary transport leading to flat density profiles at the outboard mid-plane (OMP), called 'density shoulder', in this regime.

Alternative divertor configurations (ADCs) [8] may facilitate the access to detachment. ASDEX Upgrade (AUG) is currently preparing the installation of a pair of in-vessel poloidal field (PF) coils [9] to study a series of ADCs experimentally. Analytical models and EMC3-EIRENE modelling [10] have identified several beneficial effects on heat-flux mitigation expected to occur in ADCs. Compared to the SN, SOLPS simulations predict an access to a detached divertor regime for the snowflake (SF) configuration [11] at lower upstream density and/or impurity seeding rate. In the meantime technical details of the upper divertor design have been worked out and a series of upper SN discharges have been carried out at AUG. The motivation for these experiments was to optimize the reference equilibrium and characterize the plasma parameters at the entrance point to detachment experimentally in the existing geometry. SOLPS is applied for simulating highly dissipative divertor regimes, to interpret these experiments and to extrapolate to the new configurations. Here we analyze part of the data with EMC3-EIRENE with the focus on testing recently implemented physics in the code as well as the far-SOL transport. An outstanding feature of EMC3-EIRENE is its possibility to include the 3D main chamber plasma-wall interaction that is taken into account in the work presented in this paper. In addition to that the effect of magnetic error fields on detached divertor configurations with shallow field line incidence angles—a continuation of the study carried out in reference [12] – is an important practical application of the code.

In addition to this ITER has a strong interest in applying a 3D SOL transport code tested for detached divertor conditions. In ITER symmetry-breaking resonant magnetic perturbation (RMP) [13] coils are installed in order to suppress edge-localized modes (ELMs) [14]. While in AUG ELM suppression was found only for very low pedestal collisionalities [15] and divertor conditions far from detachment, in ITER a low pedestal collisionality is expected to be compatible with a detached divertor.

And what would be the consequence, if robust ELM suppression cannot be achieved with a detached divertor? Is there a regime with sufficiently small ELMs that can be tolerated [16, 17]?

## 2. Experiments

### 2.1. Discharges

As a preparation for the operation of alternative configurations in the upper divertor of AUG a series of upper single-null (USN) H-mode discharges was carried out. The goal of these discharges was the optimization of the reference equilibrium as well as its experimental characterization in particular at the onset of detachment. Time traces of several parameters of discharges #35 921 (black) and #36 283 (green) are shown in figure 1. The plasma current of $I_P = 800$ kA figure 1(a) has a flattop phase of about 4 s. A large part of this phase is heated by $P_{NBI} = 7.5$ MW and $P_{ECRH} = 2.5$ MW, while the total radiation measured by the foil bolometers is increasing from ~5 to 8 MW figure 1(b) due to the increasing density figure 1(c), the increasing deuterium puffing and the nitrogen seeding figure 1(d). Figure 1(e) shows the thermal energy confinement time $\tau_{th}$ excluding the fast ion fraction $f_{fi}$. $f_{fi}$ was evaluated by a different method in the past leading to $H_{98}$ factors of about unity at $t = 2.2$ s and 0.8 at $t = 4.18$ while this newer evaluation yields 10–15% smaller values. Compared e.g. to a standard H-mode, for which the evaluation of $f_{fi}$ and therefore $H_{98}$ will also need to be corrected in a similar way, the confinement quality is similar. Note that despite the very different MHD activity figure 1(f) the confinement of discharges #35 921 and #36 283 is very similar.

### 2.2. Small-ELM regime & roll-over

Figure 2(a) shows the $D_\alpha$ emission integrated along the line of sight as well as over the upper outer divertor target $D_\alpha^{OT}$ normalized to its mean value $\overline{D_\alpha^{OT}}$ measured by a filtered ($\lambda_0 = 656$ nm, $\Delta\lambda_{fwhm} = 20$ nm) fast camera. Time traces of the sum over all Langmuir Probe (LP) ion saturation current measurements $I_{sat,tot} = \Sigma_i I_{sat,i}$ are shown in figure 2(b). Due to the limited coverage of the LPs this is not the total ion flux to the target, but a proxy for it. Several time intervals (around $t = 1.45, 2.2, 3.0$ and $4.0$ s) are zoomed in order to show the temporal behavior of the signal during ELMs. In contrast to #36 283, discharge #35 921 is in a small-ELM regime, where the ELM amplitude is not large anymore with respect to the average signals (cf figure 2(b)). This makes a distinction between the ELM and inter-ELM phases difficult. The ELM frequency is in the range of several hundred Hz, although the determination of an accurate value is problematic for the same reason. At about $t = 3.0$ s the smoothed $I_{sat,tot}$ (thick black line) shows a roll-over indicating the onset of particle detachment.

### 2.3. Equilibria & main chamber PWI

The magnetic equilibria computed with the cliste equilibrium code [18] of these discharges #35 921 and #36 283 (both at $t = 3.0$ s) together with the PFCs, vessel structures, gas puffing locations and selected diagnostics are shown in figure 3. In order to achieve the configurations described in references [10, 19], these equilibria were optimized in particular with respect to the outer divertor leg length as well as the plasma volume. While the PF coils of AUG are up/down symmetric, the current power supplies as well as the plasma facing components (PFC) are not, which presently limits the total plasma
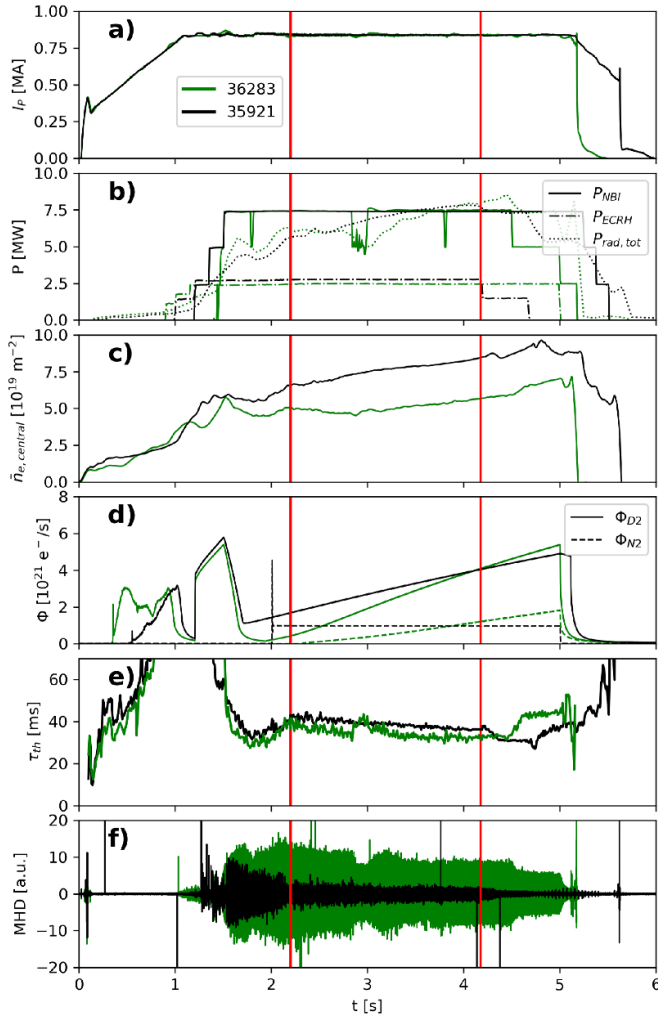
**Figure 1.** Time traces of several quantities of the AUG USN discharges #35 921 (black) and #36 283 (green). Both discharges were carried out for $B_t = +2.5$ T, i.e.in favorable drift directions for USN. An important difference is the distance of the separatrix to the limiter, $r_{u,lim} = 35$ mm $r_{u,lim} = 54$ mm for #35 921 and #36 283, respectively. Red vertical lines mark the time points for which #35 921 was simulated (cf section 3).

current to $I_P = 800$ kA and requires a rather close lower X-point defining the secondary separatrix for this USN shape. In particular at the outboard mid-plane the ICRH limiter shape is not well adapted to the separatrix: While in the upper part the clearance is large, the separatrix is only a few cm away from the limiter in the lower part. Topologically the outboard midplane is connected to the upper inner and the lower outer target when following field lines in positive $\phi$ direction (solid lines in figure 3), while it is connected to the upper outer target without interruption (dashed lines) in negative $\phi$ direction. The corresponding field line connection lengths $L_c$ are also shown in the inset of figure 3. At the secondary separatrix $L_c$ for the positive $\phi$ direction diverges, while the sudden drop of $L_c$ at $r_u = R - R_{sep} = 35$ mm and $r_u = 54$ mm for discharges #35 921 and #36 283, respectively, is due to an intersection

of the field line with the ICRH limiters. Although even the smaller value $r_u = 35$ mm is many times larger than typical near-SOL power fall-off lengths $\lambda_q^{near} \sim 3$ mm a significant amount of power is deposited onto the ICRH limiter surfaces in #35 921, as seen in figure 4(a), which shows a near infra red (spectral range 900–1200 nm) image of the antennas 1 and 2. Note that the ICR heating is switched off, and that the power is actually coming from the plasma. In particular the antenna frame of ICRH#1 that is coated with a 50 $\mu$m thick boron layer strongly emits in that spectral range. Assuming that this is thermal radiation from the surface (and not from molecular emission bands) the surface temperature is clearly above 800 °C. When the separatrix is moved further away, such that the limiter is $r_u = 54$ mm away from it in discharge #36 283 the emission is dramatically reduced (cf figure 4(b). Since the camera in discharge #35 921 is saturated it is not possible to determine an absolute heat flux from them. However, it is likely that heat fluxes in the MW m$^{-2}$ range are required to explain the observation.

The equilibria were compared to those computed by the IDE equilibrium code [20] that includes additional constraints from edge plasma profile measurements as well as current diffusion. According to IDE the separatrix is even further away from the limiter, i.e. $r_u = 43$ mm at $t = 2.2$ s and $r_u = 70$ mm at $t = 4.18$ s. The positions of the leading edges of the ICRH limiters were measured in the $z = +450$ and the $z = -450$ planes as shown by the red crosses in figure 3. According to that measurement, the limiters protrude their nominal position by less then 1 mm.

### 2.4. Power deposition profiles

Excluding that both equilibrium codes underestimate the radial position of the separatrix at the outboard midplane in the cm range, the only explanation for substantial heat fluxes 35 mm away from the separatrix is either a single global (time averaged) power fall-off length substantially larger than 3 mm, or an enhanced fall-off length in the far-SOL, different from the near-SOL one. Fortunately, the open divertor- and viewing geometry (cf black lines in figure 3) allows heat flux measurements up to a distance of $s - s_{OSP} \leq 250$ mm from the separatrix along the target, corresponding to an upstream interval of about 90 mm. Similar settings of the IR camera (acquisition rate 666 Hz, spatial resolution $ds = 2.18$ mm pixel$^{-1}$) as those in reference [21] were chosen. For the evaluation of a heat flux profile from the raw data a newly implemented version [22] of the THEODOR heat transport code [23] was applied. These profiles are then compared to a 'standard' power deposition profile $q_{\perp}^{std}(s, q_0, \lambda_q, S, q_{BG})$ as defined by equation (2) in reference [2], where $\lambda_q$ and $S$ define the SOL power fall-off length and the divertor broadening parameter, respectively[7]. $q_0$ is the heat flux at the target coordinate $s = s_{OSP}$ of the outer strike

---

[7] Note that here we define the $S$ parameter at the outboard mid-plane, i.e. by a factor $f_x^{-1}$ different to that in [2].
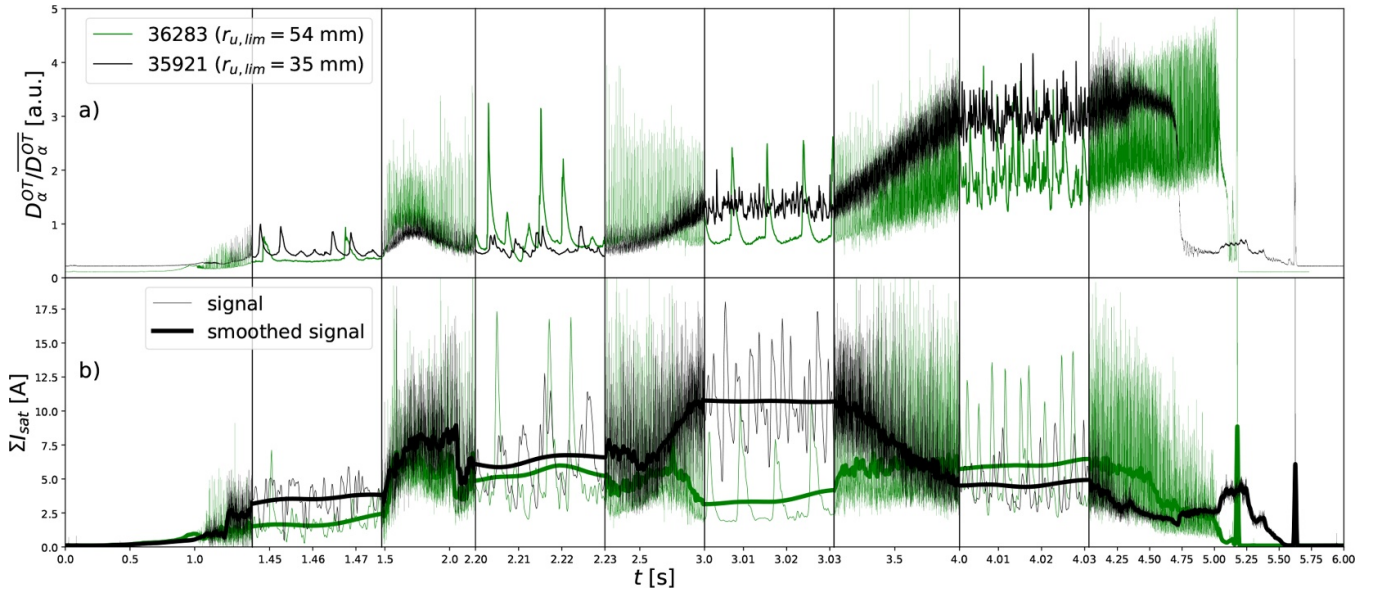
**Figure 2.** $D_\alpha$-emission from the upper outer divertor normalized to its average value recorded by a filtered ($\lambda_0 = 656$ nm, $\Delta\lambda_{fwhm} = 20$ nm) fast camera (a) and sum over the outer divertor ion saturation current measurements, $\Sigma I_{sat}$, from the divertor Langmuir Probes (b). Several time intervals (around $t = 1.45, 2.2, 3.0, 4.0$ s) are zoomed in order to show the temporal behavior of the signal during ELMs. In contrast to #36 283, discharge #35 921 is in a small-ELM regime, where the ELM amplitude is not large anymore with respect to the inter-ELM signals. The $\Sigma I_{sat}$ signal shows a roll-over for discharge #35 921 around 3 s indicating the onset of particle detachment.

point if $S$ was zero and $q_{BG}$ a constant offset. Note that in contrast to reference [2], where *inter-ELM* profiles are analyzed, here a distinction between the ELM and inter-ELM phases was not possible (cf section 2.2) and so we study the time-averaged quantities denoted by $\bar{q}_0, \bar{\lambda}_q, \bar{S}$ and $\bar{q}_{BG}$ here. While an explicit plot is not shown here for the sake of brevity, the quality of the best fit quantified by the root of the mean square deviation is $\Delta = 7.8$ kW m$^{-2}$ for $\bar{\lambda}_q = 6$ mm, $\bar{S} = 2$ mm, $\bar{q}_0 = 6.6$ MW m$^{-2}$ and a finite $\bar{q}_{BG} = 126$ kW m$^{-2}$. If this was the upstream value for $\bar{\lambda}_q$ the parallel heat flux at the limiter 35 mm away from the separatix would have decayed to $e^{-35/6} = 0.3$ % of the value at the separatix.

A significantly better fit with $\Delta = 4.3$ kW m$^{-2}$ is achieved by fitting a sum of two such standard power flux profiles

$$q_\perp^{sum} = q_\perp^{std}(s, \bar{q}_0^{near}, \bar{\lambda}_q^{near}, \bar{S}) + q_\perp^{std}(s, \bar{q}_0^{far}, \bar{\lambda}_q^{far}, \bar{S}) \quad (1)$$

with different $\bar{q}_0$, different $\bar{\lambda}_q$, but equal $\bar{S}$ parameters and $\bar{q}_{BG}^{near} = \bar{q}_{BG}^{far} = 0$, as shown by the dashed black curve in figure 5. The near and far SOL components with $\bar{\lambda}_q^{near} = 3.8$ mm and $\bar{\lambda}_q^{far} = 25$ mm are shown in green and blue, respectively. While the ratio of these two lengths is about $\bar{\lambda}_q^{far}/\bar{\lambda}_q^{near} = 7$ the ratio $\bar{q}_0^{far}/\bar{q}_0^{near}$ approximately has the inverse value. Since the integrated power $P = \int_{-\infty}^{\infty} 2\pi R q_\perp(s) ds$ for the standard power deposition profile $q_\perp = q_\perp^{std}$ is given by $P^{std} = 2\pi R q_0 \lambda_q$, about the same power $P^{near} = 732$ kW and $P^{far} = 681$ kW is contained in the two contributions. At the outboard midplane the heat flux profile is still described by equation (1), but with $S = 0$, which decays at the limiter position to $e^{-35/25}/(7+1) = 3$ %, i.e. about ten

times more than for the single standard profile fit. IR measurements with enhanced temporal resolution but reduced spatial coverage in discharge #37 464 that has a lower density and larger ELMs indicate that the second fall-off length is caused by the ELMs.

With increasing line integrated density and nitrogen puffing rate at later time points of the discharge the outer target is approaching power and particle detachment. The first (power detachment) is seen by a strong reduction of the peak values of the IR measurements for $t = 2.8$ s and $t = 4.0$ s (brown and gray curves in figure 5, right). Interestingly, the profiles can still be fitted by equation (1) with the same $\bar{\lambda}_q^{near}, \bar{\lambda}_q^{far}$ and $\bar{S}$ values, but with $\bar{q}_{0,\perp}^{near}$ approaching zero describing the reduction of the near-SOL fluxes. Whether this is a universal behavior and if so which physical model can describe this empirical finding are open questions for future investigations. The important finding in this context is that the power flux profile before and during detachment shows a significant far-SOL component that contains a substantial fraction of the power leaving the separatrix and should be taken into account in power exhaust extrapolations.
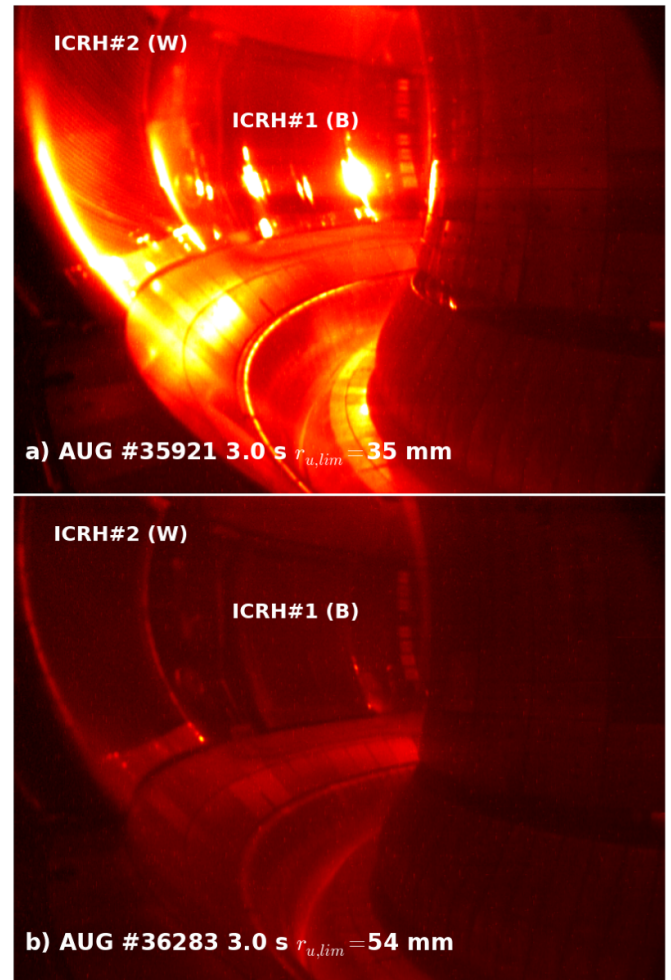
## 3. Simulations

### 3.1. Code version & geometry

In order to interpret the experimental findings, simulations with the Edge Monte-Carlo 3D (EMC3) - EIRENE code package were carried out. EMC3 solves Braginskii-like fluid equations for the plasma and is described in detail in references [24, 25], while EIRENE [26] treats the neutral particle
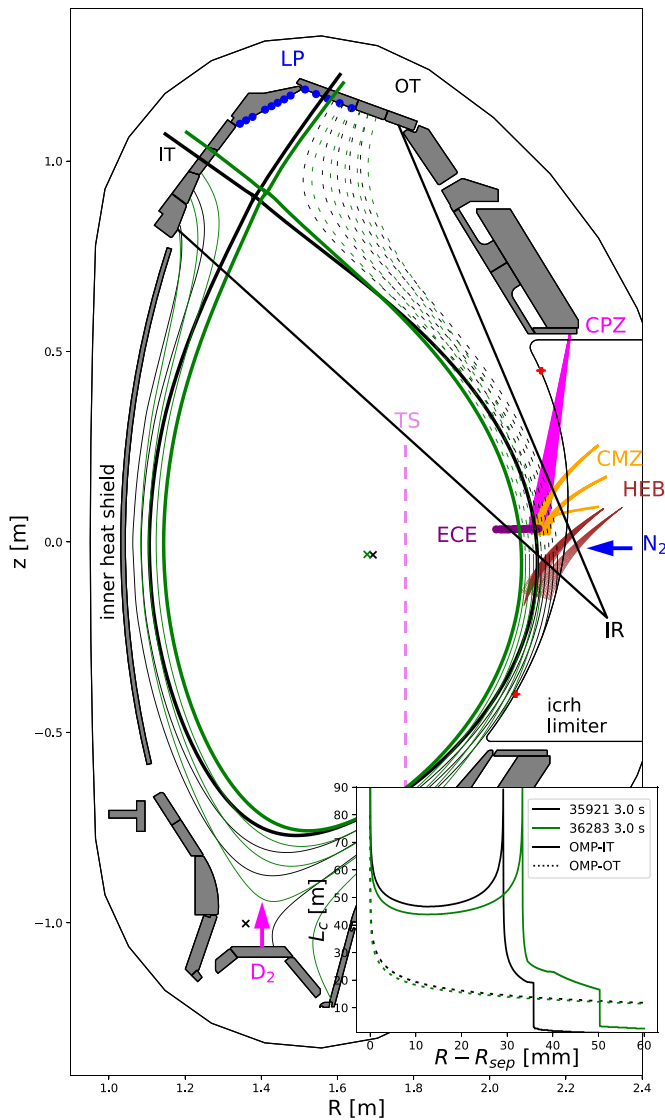
**Figure 3.** Poloidal cross section of ASDEX Upgrade. The magnetic equilibria of discharges #35 921 and #36 283 are shown in black and green, respectively. Several diagnostics are included, IR thermography (IR, black), the thermal He- beam (HEB, brown),the Langmuir probes (LP, blue dots), core Thomson Scattering (TS, violet), Electron Cyclotron Emission spectroscopy (ECE, purple) and the poloidal (CPZ, magenta) and toroidal (CMZ, orange) Charge Exchange Recombination Spectroscopy. The deuterium and nitrogen gas puffs are indicated by the magenta and blue arrows, respectively. The inset shows the field line connection length from the outboard midplane to the upper inner (solid lines) and upper outer (dashed lines) targets for the two equilibria.



**Figure 4.** Near infra-red image of the AUG main chamber with a distance of (a) 35 mm and (b) 54 mm between the separatrix and the antenna surface. The camera is sensitive in the spectral range $\lambda = 900\ldots 1200$ nm. Note that the ICR heating is switched off in both cases.

transport kinetically. Both codes apply Monte-Carlo techniques to solve the equations numerically. While an outstanding feature of EMC3-EIRENE is its capability to handle 3D fields and/or 3D PFCs, a satisfactory description of the asymmetry between the inner and outer divertor target in AUG as well as the detached divertor state was not achieved so far with EMC3-EIRENE. This was attributed to the lack of volumetric recombination and drifts in the standard code version applied until now. Both drifts and recombination were required to describe the experimental data in AUG

LSN by means of SOLPS [27]. While substantial progress is being made by IPP Greifswald in computing currents and the electric potential in EMC3 [28] – an obvious prerequisite to implement drifts—volumetric recombination (including radiative-, three-body- and molecular-assisted recombination processes) has recently been implemented by the colleagues from the University of Wisconsin and has now been applied for the first time at AUG in this study[8]. A reduction of power and particle fluxes to the targets with increasing upstream density—as characteristic for detachment—has been observed in W7X even without volumetric recombination (and drifts) [29].

A crucial requirement to set-up an EMC3-EIRENE run is a computational grid (consisting of about $40 \times 500 \times 10$ grid cells in radial, poloidal and toroidal directions, respectively). The grid not only discretizes the computational domain, but

---

[8] Registered users can find the code on the gitlab server https://gitlab.mpcdf.mpg.de/emc3-eirene/. For this study the versions 743cdc92 (EMC3) and 6b078 936 (EIRENE) were used.
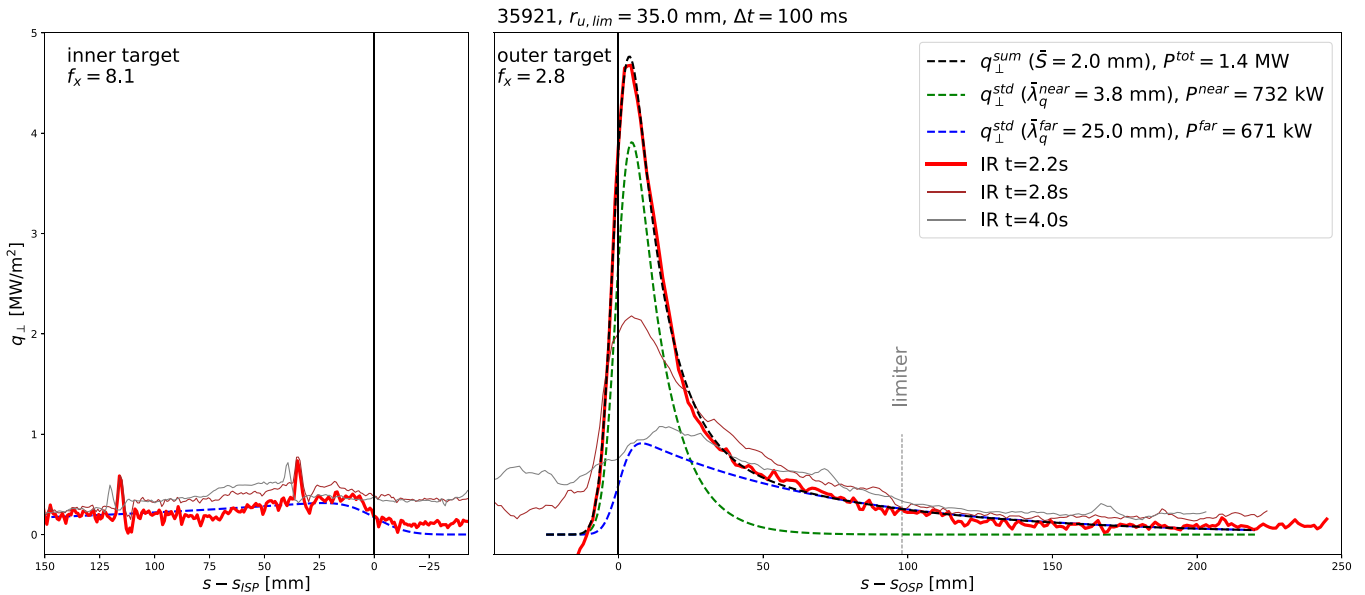
**Figure 5.** Power fluxes averaged over 100 ms, i.e. several small-ELM cycles, at different time points of the discharge #35 921. While the inner divertor is strongly detached from an early phase of the discharge on, the power detachment is getting stronger over the time due to the increasing line averaged density.

also defines the magnetic field configuration. Here, as in a previous study (cf figure 1 of reference [30]) we make use of the freedom not to align radial surfaces of the grid to the poloidal flux in the far-SOL region ($\rho > 1.033$) allowing a coverage of the entire edge plasma from $\rho_{pol} = 0.95$ to even remote PFCs ($\rho_{pol} = 1.38$) by a topologically simple grid including the main chamber limiters. The equilibria of #35 921 at $t = 2.2$ s and $t = 4.18$ s were chosen. The toroidal extension of the grids is $\Delta\phi = 22.5°$, i.e. 1/16 of the toroidal circumference, assuming a 16 fold symmetry. While in the toroidal intervals, where the ICRH antennas are located, $\phi = 18° \ldots 90°$ and $\phi = -162° \ldots -90°$, this is close to reality, the intervals in between are equipped with 4 slightly retracted auxiliary limiters, where the approximation is not as good.

In the following sections we will now discuss the radial up- and downstream profiles as well as the related transport coefficients. Other input parameters like the power and particle sources and sinks in the simulation are discussed later on in sections 3.5 and 3.6 discussing the power and particle balances.

### 3.2. Up- and downstream profiles

Radial profiles of several quantities are shown in figure 6 for $t = 2.2$ s. The plots on the left side show the upstream profiles at the outboard mid-plane, while *target* profiles are shown on the right, where the red and blue colors distinguish the inner and outer targets, respectively. In addition to the time (and small-ELM cycle) averaged upstream $n_e$, $T_e$ and $T_i$ profiles the corresponding time averaged diffusion coefficients $\overline{D}$, $\overline{\chi}_e$ and $\overline{\chi}_i$, assumed to be constant on flux surfaces, are also given

by the green curves corresponding to the right scales of left column plots. These coefficients were adapted in an iterative procedure with the goal to find a simultaneous match of the up- and the downstream profiles to the experimental data. Since we are mostly interested in the conditions at the target a stronger emphasis was put on the match of the downstream profiles, while accepting a certain mismatch upstream. Probably a better match both up- and downstream could be obtained when relaxing the assumption of constancy of $\overline{D}$, $\overline{\chi}_e$ and $\overline{\chi}_i$ along the flux surface. Indications for a poloidal asymmetry of the transport across the LCFS are in fact found in several Tokamaks in the world [31, 32] and explained by the 'bad' curvature at the OMP. In order to keep the assumptions reasonably simple, however, we decided not to allow this degree of freedom. Another assumption that may be questioned is the diffusive nature of the transport. Possibly a significant or even dominant contribution to the transport can be attributed to convective processes. In any case it is likely that the realistic transport cannot be parameterized neither by one or the other (cf figure 1 from reference [33]) but would require a time dependent and non-local treatment of the (turbulent) transport, which is not provided by EMC3. However, since we are interested in the time averaged profiles it will always be possible to find effective diffusion coefficients that describe the fluxes. The same argumentation justifies the inclusion of the time-averaged transport caused by the small ELMs in the transport coefficients. Note the *different* approach e.g. in reference [34], where time-*dependent* transport coefficients were used to describe the transport of the ELMs.

The upper left plot of figure 6 includes a third scale (gray) indicating the neutral particle flux across the closed magnetic surfaces in the confined region. All the EMC3-EIRENE (in-
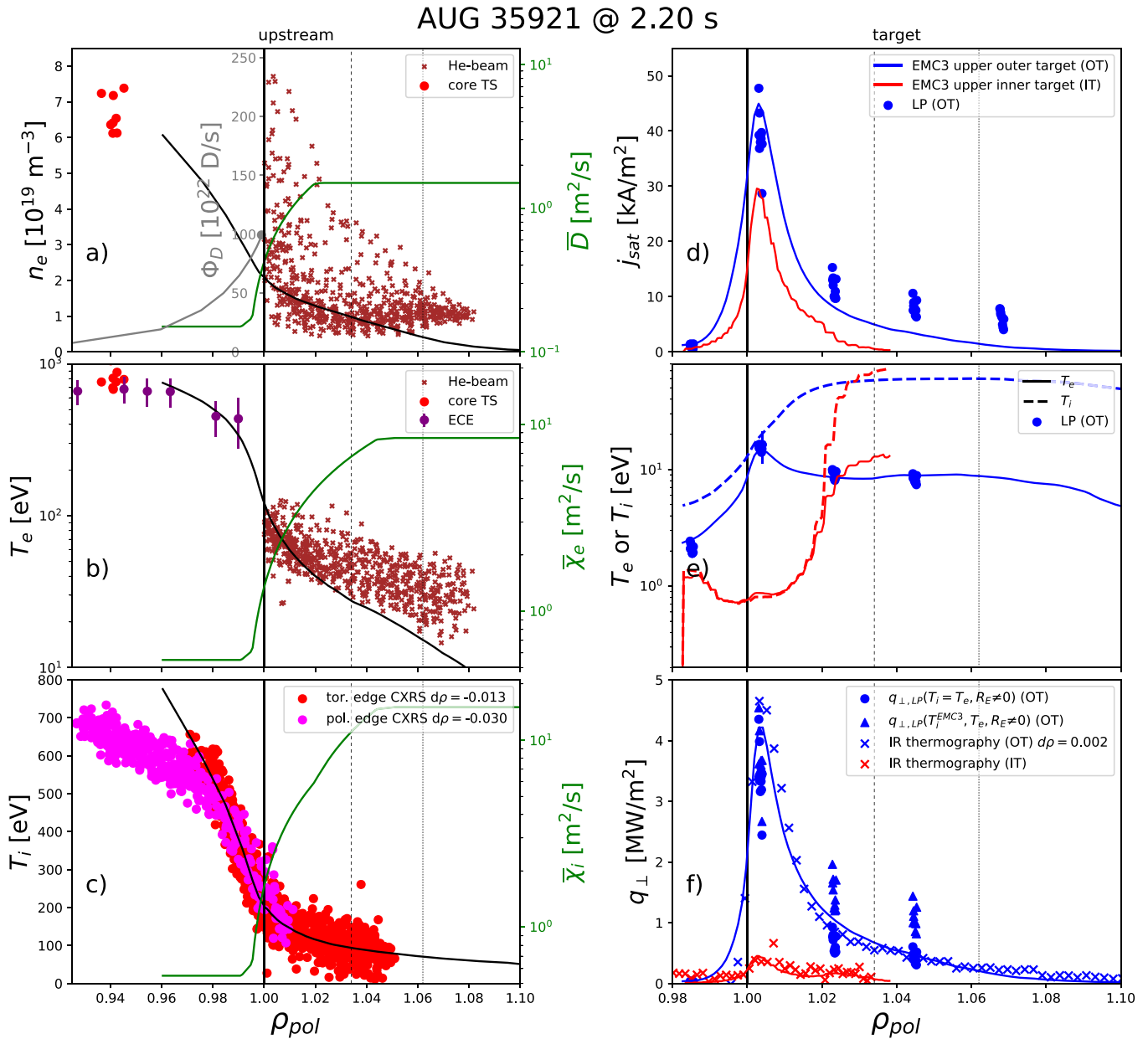
**Figure 6.** Radial profiles of various quantities computed by EMC3-EIRENE for discharge #35 921 at $t = 2.2$ s. Upstream quantities are plotted on the left, and target quantities on the right. The simulation (solid lines) is compared to time/small-ELM averaged quantities from various diagnostics (data points). The time averaged transport coefficients $\overline{D}$, $\overline{\chi_e}$ and $\overline{\chi_i}$ are given by the green curves. The dashed and dotted vertical lines indicate the positions of the secondary separatrix and the limiter, respectively. More details concerning this plot are found in section 3.2.

and output) profiles are shown by solid lines, while experimental data is shown by discrete symbols.

For geometrical reasons the Li-beam diagnostics, commonly used to measure upstream density profiles in AUG, can only measure within the far-SOL ($\rho_{pol} \geq 1.06$). Furthermore, the data is strongly perturbed by the neutral gas recycled at the limiter as well as due to the seeded nitrogen, so that the data is not shown here. The recently installed He-beam diagnostics [35, 36] measuring $n_e$ and $T_e$ simultaneously, however, covers the near-SOL up to the separatrix. Since it relies on a line-ratio- instead of an attenuation measurement it is less affected by the neutral gas. Nevertheless, the data in

(figure 6(a) and (b)) also shows a strong scatter, which likely reflects the intermittent and filamentary transport in the SOL. Furthermore the absolute value and the decay length of the profiles are not fully benchmarked for the given scenario and might therefore contain additional uncertainties. The transport coefficients and the boundary condition for the density at the separatrix (here $n_{e,sep} = 2.1 \times 10^{19}$ m$^{-3}$) are adapted in the simulation, such that the upstream SOL profiles match these $n_e$ and $T_e$ measurements as shown by the brown crosses in (figure 6(a) and (b)). In addition to that the profiles inside the LCFS are adapted to the 'core'-Thomson-scattering (red data points) and the ECE diagnostics (purple data points with

error bars). The $T_i$ profiles inside and outside the LCFS are adapted to the $T_i$ measurements from the charge-exchange recombination spectroscopy (CXRS, red and magenta colored data points), that were slightly shifted by the $d\rho$ values given in the figures.

At the outer target the $j_{sat}$ and $T_e$ profiles were measured by the divertor (triple) Langmuir Probes (LP) as shown by the blue data points in (figure 6(d) and (e)). While $T_e$ matches the simulation data within a few percent, the experimental $j_{sat}$ exceeds the simulation by a factor of two in the outer SOL ($\rho \geq 1.02$). The LPs are not covering the position of the inner divertor leg, such that no experimental $j_{sat}$ and $T_e$ data is available there. An excellent spatial coverage, including the outer and inner target, however, is achieved with infra-red thermography (cf blue points and orange lines in figure 3. The data is shown by the red and blue cross-symbols in figure 6(f) for the inner and outer target, respectively.

After crossing the potential drop of about $2.85 \cdot T_e$ the ions and electrons have energies $E_i = \gamma_i T_i + 2.85 T_e$ and $E_e = (\gamma_e - 2.85)T_e$, respectively. For the heat sheath transmission factors the same values $\gamma_i = 2.5$ and $\gamma_e = 4.5$ were chosen as in the EMC3 simulation. According to [37] the deposited heat at the target is given by

$$q_{\perp,LP} = [E_i \cdot (1 - R_E(E_i)) + E_e + E_{i,d}] \, |j_{sat}/q_e|, \quad (2)$$

where $R_E$ is the energy reflection coefficient (cf equation 6 from reference [37]), here for deuterium on tungsten. Assuming $T_i = T_e$ as often done, when analyzing LPs the $q_{\perp,LP}$ match the thermography data within $\sim 10\%$ as shown by the blue dots in figure 6(f). In comparison to that the blue triangles in the same plot show equation (2) taking the $T_i$ values from the simulation, which are clearly above the values measured by thermography for the outer SOL. An explanation for the discrepancy of both $j_{sat}$ and $q_{\perp,LP}$ in the outer SOL might be the finite concentration of impurities there ($c_Z \sim 30\%$). In the code the impurity radiation is taken into account in the energy equation, while their contribution to the density, charge and momen[4] are neglected in the continuity equation. Here a full multi-fluid treatment would be desirable.

### 3.3. In- out asymmetry

What is remarkable is also that the asymmetry between the inner and the outer target of the $q_\perp$ profile is well reproduced. For purely geometrical reasons an asymmetry between the deposited heat fluxes of $f_{x,IT}R_{OT}/(f_{x,OT}R_{IT}) = 8.1 \cdot 1.54 \, \text{m}/(2.8 \cdot 1.26 \, \text{m}) = 2.4$ is expected, however, the measured asymmetry of the peak values of a factor of ten is substantially larger than that. In forward field direction as in the experiment ($B_t = +2.5$ T in USN) the asymmetries are commonly attributed predominantly to the diamagnetic and $E \times B$ drifts [38] as well as the curvature drift leading to a poloidal asymmetry of the power and particle transport across the LFCS. Since drifts are not included in the code so far, this raises the question whether the (divergences of the) drift

terms are small with respect to the (divergence of) the other fluxes under the present (cold) divertor conditions, whether the terms are large but cancel each other out or if the interaction with the ICRH limiter is predominantly responsible for the in-out asymmetry. It might for example be, that the small ELMs cause a poloidally asymmetric transport that cancels the one caused by the drifts. In order to investigate this question another pair of discharges (#36 243 and #36 245) for both toroidal field directions was performed, with the limiter further away from the plasma: While in both cases the asymmetry is larger than the one expected from geometry, the ratio of the peak values at the inner and outer targets is a bit larger (5.1) in favorable field direction (#36 243, $B_t = +2.5$ T) than that (3.5) for the unfavorable drift direction (#36 245, $B_t = -2.5$ T). An asymmetry is seen more clearly by a (fast) camera equipped with a $D_\alpha$ filter that observes a strong emission between the inner target and the inner heat shield in favorable drift direction, indicating the existence of a high field side high density region similar to the one observed in LSN [39]. For the unfavorable drift direction the $D_\alpha$ emission is much more symmetric. Unfortunately not only the limiter separation for the pair #36 243/5 was different from that in #35 921 but also the density lower by $\sim 15\%$, such that the effect cannot be attributed unambiguously to the interaction with the limiter alone. A reference simulation with an artificially prolonged inner divertor leg, a smaller flux expansion $f_x = 4.0$ and a more open divertor geometry showed a far smaller in- out asymmetry. So while drift effects are present, the in-out power asymmetry observed under the conditions investigated here, seems to be dominated by the large difference in flux expansion and/or the divertor closure.

### 3.4. Detachment

Note that the electron temperature at the inner target has collapsed in the near-SOL region to values around 1 eV, where detachment is expected to occur. Comparing the radial profile of the total pressure $p_{tot} = n_e (T_e + T_i) (1 + M^2)$ upstream and downstream (cf figure 11(a) a loss of $p_{tot}$ is observed for the inner target already for $t = 2.2$ s, indicating that detachment has indeed set-in there. So the asymmetry between the inner and outer target is likely related to their different detachment state.

The same analysis as for $t = 2.2$ s was carried out for $t = 4.18$ s as shown in figure 8. At that time point the gas puff, the separatrix density (now $n_{e,sep} = 2.5 \times 10^{19} \, \text{m}^{-3}$) and the emitted total radiation are significantly higher. In order to fit the upstream density and temperature profiles the transport coefficients (green curves in figures a-c) had to be adapted accordingly. This results in a collapse of the simulated $T_e$ at both targets as well as of the target power fluxes (cf figures 8(e) and (f)). The *measured* peak $T_e$ and $q_\perp$ values also decrease dramatically to 3.5 eV and 1 MW m$^{-2}$, respectively. Since the error bar for low $T_e$ measurements is of the same order of magnitude as its absolute value, the temperature measurement alone is not in contradiction to the sub-eV range values suggested by the simulation. However, the peak power flux of the order of $q_{\perp,IR} = 1$ MW m$^{-2}$ seen

by IR thermography at the outer target are more consistent with electron temperatures in the low eV range. An alternative explanation for the significantly larger $q_{\perp,IR}$ values compared to the simulation and the probes would also be the deposition of power by radiation and charge-exchange neutrals. A quantitative treatment of these processes, however, would require a radiation transport model including photo ionization and is left for future work. So generally the detachment process is well reproduced by EMC3-EIRENE, but maybe even slightly overestimated. Note that due to the high collisionality electrons and ions are now strongly coupled and therefore $T_e = T_i$. A strong loss of the total pressure is also seen in figure 11(b), which is a characteristic signature of detachment.

### 3.5. Power balance

An overview of the power fluxes contributing to the power balance is given in (table 1(a)) and graphically represented in figure 7(a). The plasma is heated by $P_{NBI} = 7.5$ MW of neutral beam injection and by $P_{ECRH} = 2.5$ MW of electron cyclotron resonance heating (ECRH). Since ion cyclotron resonance heating (ICRH) is switched-off (except for a short blip) and ohmic heating negligible the total heating power is $P_{heat} = 10$ MW. A small part of that $P_{MHD} = -dW_{MHD}/dt$ changes the internal energy $W_{MHD}$ of the plasma obtained from the equilibrium reconstruction based on experimental data. Tomographic inversion of bolometry shows that the radiation *inside* the inner simulation $P_{isb}$ boundary for the plasma located at $\rho_{pol} = 0.95$, is approximately $P_{isb} \sim -2$ MW, leaving $P_{heat} + P_{isb} + P_{MHD} \sim 8$ MW as input power for the simulation. This power is assumed to be equally distributed between the ions and electrons. The rest of the measured radiation emitted from the pedestal region ($0.95 \leq \rho_{pol} \leq 1$), $P_{N,ped}$, and from the SOL (which here includes the private flux region), $P_{N,SOL}$, is attributed to the Nitrogen injected from the outboard midplane into the vessel (cf figure 3) as well as the excited and recombining neutral deuterium in the SOL $P_{D,SOL}$. Radiative fractions $f = |P_{isb} + P_{N,ped} + P_{N,SOL} + P_{D,SOL}|/(P_{heat} + P_{MHD})$ between 62 and 76 % are achieved. While for $t = 4.18$ s the total radiation power is exactly the one measured by bolometry, the total radiation is assumed to be 10% higher than the measurement for $t = 2.2$ s, which is well within the error bars. In the simulation the impurity source is described formally as chemical sputtering, where the sputtering coefficient is controlled by EMC3 such that the total radiation in the computational domain is matched. For computing the radiation distribution this assumption is not as bad as it might seem at the first sight, because it depends mostly on the locations in the plasma where $T_e$ is in the adequate interval and not as much on the source position. In fact even a corona model assuming a constant nitrogen concentration on the $n_e$ and $T_e$ background computed by EMC3 and that the distribution of the nitrogen ionization stages is given by the local balance of electron impact ionization and radiative recombination shows a very similar distribution of the radiation. The assumption is also consistent with the

**Table 1.** Power- and particle balances for discharge #35 921 simulated by EMC3-EIRENE. The meaning of the quantities is described in sections 3.5 – 3.7 and a graphical representation is given in figure 7. Note the different units treating the particle balance of the plasma as a whole (part b) and the confinement region in particular (part c). Also note that due to the assumed 16-fold symmetry the fluxes received by an individual limiter are by a factor of 16 smaller than the ones given here.

|  | $t = 2.20$ s | $t = 4.18$ s |
|---|---|---|
| **a) power balance (MW)** | | |
| $P_{heat}$ | 10.00 (100%) | 9.99 (100%) |
| $P_{MHD}$ | –0.30 (–3%) | 0.29 (3%) |
| $P_{isb}$ | –2.28 –23%) | –1.54 (–15%) |
| $P_{N,ped}$ | –0.29 (–3%) | –1.09 (–11%) |
| $P_{N,SOL}$ | –3.11 (–31%) | –4.35 (–44%) |
| $P_{D,SOL}$ | –0.36 (–4%) | –0.80 (–8%) |
| $P_{OT}$ | –2.26 (–23%) | –0.41 (–4%) |
| $P_{IT}$ | –0.52 (–5%) | –0.33 (–3%) |
| $P_{lim}$ | –0.46 (–5%) | –0.85 (–8%) |
| $P_{IHS}$ | –0.08 (–1%) | –0.11 (–1%) |
| $P_{EL,CX}$ | –0.10 (–1%) | –0.70 (–7%) |
| $P_{other}$ | –0.24 (–2%) | –0.12 (–1%) |
| **b) particle balance whole plasma ($10^{21}$ s$^{-1}$)** | | |
| $\Phi_{puff}$ | 1.6 (0.6%) | 4.0 (1.1%) |
| $\Phi_{NBI}$ | 1.0 (0.4%) | 1.0 (0.3%) |
| $\Phi_{pump}$ | –0.2 (–0.1%) | –0.7 (–0.2%) |
| $\Phi_{abd}$ | –2.4 (–1.0%) | –4.3 (–1.2%) |
| $\Phi_{ion}$ | –247 (–100%) | –354 (–100%) |
| $\Phi_{recomb}$ | 44 (18%) | 120 (34%) |
| $\Phi_{OT}$ | 89 (36%) | 121 (34%) |
| $\Phi_{IT}$ | 100 (40%) | 71 (20%) |
| $\Phi_{lim}$ | 10 (4%) | 36 (10%) |
| $\Phi_{IHS}$ | 1.4 (0.6%) | 2.8 (0.8%) |
| $\Phi_{rest}$ | 3.0 (1.2%) | 2.5 (0.7%) |
| **c) particle balance confinement region ($10^{20}$ s$^{-1}$)** | | |
| $\Phi'_{ion}$ | –109.7 (–100%) | –233.1 (–100%) |
| $\Phi'_{puff}$ | 1.5 (1%) | 1.5 (1%) |
| $\Phi'_{NBI}$ | 9.5 (9%) | 9.4 (4%) |
| $\Phi'_{recomb}$ | 0.3 (0%) | 62.1 (27%) |
| $\Phi'_{OT}$ | 58.4 (53%) | 70.9 (30%) |
| $\Phi'_{IT}$ | 6.7 (6%) | 27.4 (12%) |
| $\Phi'_{lim}$ | 23.4 (21%) | 52.6 (23%) |
| $\Phi'_{IHS}$ | 4.7 (4%) | 7.2 (3%) |
| $\Phi'_{rest}$ | 5.1 (5%) | 2.1 (1%) |

experiment, where a second discharge (#35 922) with identical discharge parameters and the same amount of nitrogen puffing but a different injection position in the private flux region, shows only a slightly different radiation distribution and almost exactly the same IR thermography power deposition pattern [40].

The inner and outer targets, the inner heat shield and the ICRH limiters receive $P_{IT}$, $P_{OT}$, $P_{IHS}$ and $P_{lim}$, respectively. Note that an individual limiter receives only one $16^{th}$ of this value due to the (simplifying) assumption of a 16-fold symmetry (cf section 3.1). For $t = 4.18$ s this is $P_{lim}/16 = 50$ kW which is deposited onto an area of the order of 0.02 m$^2$. The
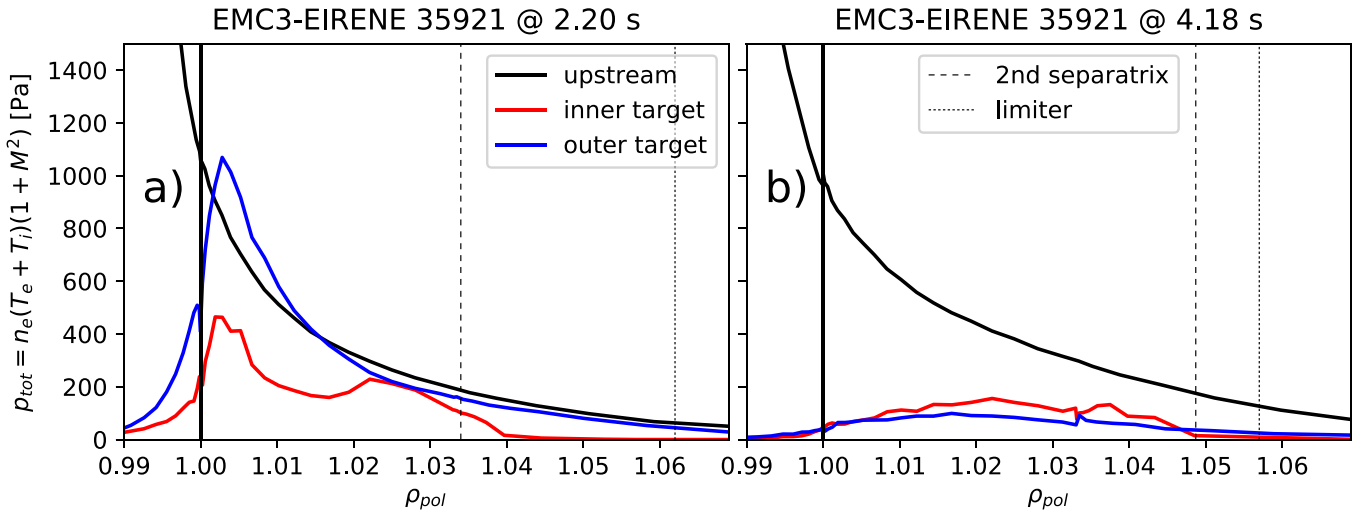
**Figure 7.** Total pressure at the outboard midplane (upstream) and at the inner and outer targets computed by EMC3-EIRENE for two different phases of discharge #35 921. While for $t = 2.2$ s only the inner target shows a loss of the total pressure, both targets show a pressure loss for $t = 4.4$ s. The pressure loss is a signature of detachment.

resulting power flux densities are then of the order of 2.5 MW m$^{-2}$, which explains the glowing limiters. Power flux densities to the limiters of similar magnitude were found in 2004 in a different AUG discharge [41].

The deposited powers include the contribution from the atomic ionization and the molecular dissociation energy $E_{i,d} = E_{ion} + E_{diss}/2 = 15.6$ eV per ion. Since this energy was taken previously from the electrons, the total power going into ionization and molecular dissociation does not appear explicitly in the power balance. It can easily be computed—if of interest—by multiplying $E_{i,d}$ with the total ionization rate (cf section 3.6) $\Phi_{ion}$. A contribution from the neutrals that *does* appear in the power balance is the power $P_{EL,CX}$ transferred from the plasma to the neutral gas via charge exchange and elastic collisions. $P_{other}$ contains marginal contributions from remote PFCs and numerical inaccuracies originating from the finite grid resolution.

### 3.6. Particle balance

While the heating power is the only and therefore the dominant source of energy, the situation is a bit more complicated for the particles. The particles injected by the gas puff $\Phi_{puff}$ and the neutral beam $\Phi_{NBI}$ only constitute a small fraction ($\leq 2\%$) of the total number of ionization processes $\Phi_{ion}$ in the plasma. The fluxes in (table 1(b)) show the different contributions $\Phi_i$ (where the labels $i$ represent the same ones as in previous section) as well as the normalized values $\Phi_i/|\Phi_{ion}|$ in brackets. Positive numbers represent neutral particles going into or being born by recombination processes inside the computational domain, while negative ones represent neutral particle sinks. Due to the large distance of the cryo-pump from the high neutral compression region in the upper divertor the pumping rate $\Phi_{pump}$ computed by EIRENE assuming a typical sticking probability of $\sim$10% is clearly below the external sources from the gas puff and the NBI. Due to the sensitive dependence

of the downstream plasma parameters on the upstream conditions the separatrix density is kept fixed in the simulation such that EMC3 converges fastest. The code then fulfills an 'external' particle balance $\Phi_{NBI} + \Phi_{puff} + \Phi_{pump} + \Phi_{abd} = 0$ by assuming that a small fraction of the total ionization flux $\Phi_{abd}/\Phi_{ion}$ is absorbed by or released from the wall. As shown in (table 1(b)) rather large fluxes $|\Phi_{abd}| \lesssim 4 \times 10^{21}$ 1 s$^{-1}$ nuclei per second or about $10^{22}$ particles after the 5 s long discharge are absorbed in the machine interior. Assuming that deuterium can penetrate the surface-near bulk tungsten at most 10 nm and that the density of lattice defects allowing the storage of these particles is at most 1%, it is unlikely that these amounts of particles are stored in the surface-near bulk tungsten layers. However, very similar amounts of stored particles have been found experimentally in gas balance measurements in LSN discharges in AUG with all-W (coated) PFCs [42] justifying the assumption. In any case it might be possible to fulfill the external particle balance with smaller values of $\Phi_{abd}$ by more realistic assumptions on the neutral particle conductance and/or the transport model in general.

Apart from the external balance an 'internal' balance $\Phi_{ion} + \Phi_{recomb} + \Phi_{OT} + \Phi_{IT} + \Phi_{lim} + \Phi_{IHS} + \Phi_{rest} = 0$ is fulfilled for the recycling, where $\Phi_{recomb}$ is the recombination rate of ions in the volume and $\Phi_{IT}$, $\Phi_{OT}$, $\Phi_{lim}$, $\Phi_{IHS}$ and $\Phi_{rest}$, the fluxes at the inner and outer targets, the ICRH limiter, the inner heat shield and other remaining PFCs, respectively. These terms are summarized in the second part of (table 1(b)) and represented in figure 7(b).

### 3.7. Particle fueling

In addition to this it is instructive to analyze the particle balance for the confinement region separately. The probability of a neutral particle to reach the last closed flux surface (LCFS) depends sensitively on their energy, starting nobreak-position and the local mean-free path for ionization in the SOL.

## AUG 35921 @ 4.18 s
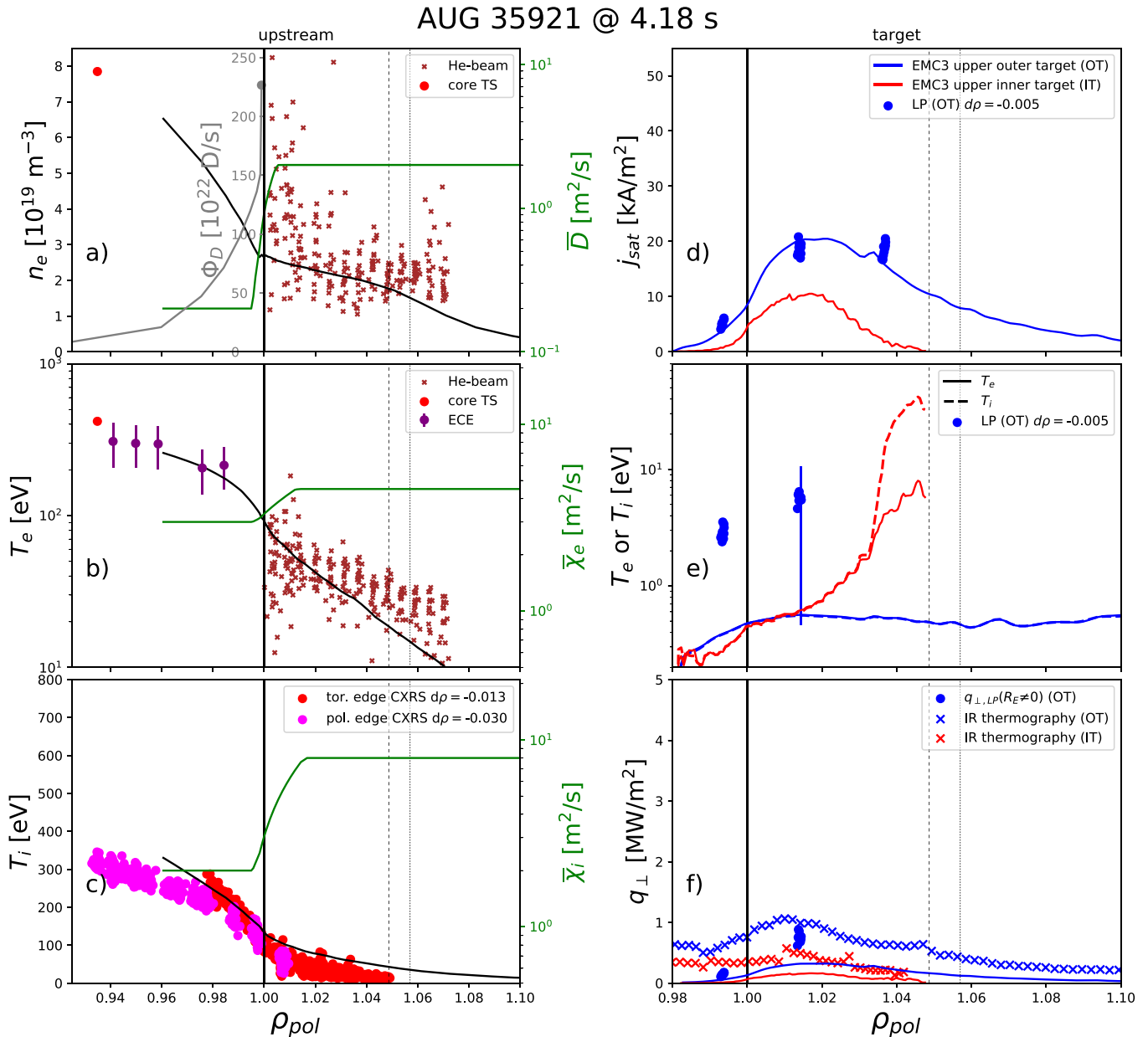


**Figure 8.** Same as figure 6, but at a later time point $t = 4.18$ s in the discharge. Due to the higher gas puff, density and radiation both targets are in detachment.

Comparing the total ionization rate in the confined region $\Phi'_{ion}$ to the one for the entire plasma $\Phi_{ion}$ it is found that only about $\Phi'_{ion}/\Phi_{ion} \sim 5\%$ of the particles cross the LCFS. We refer to these fluxes as 'fueling'. Source resolved particle balances for the confinement region alone for the two time points in discharge #35 921 are given by the $\Phi'_i$ values found in (table 1(c)) and figure 7(c), where the labels have the same meaning as in previous section 3.6. A very interesting finding is that the inner and outer targets are predominantly responsible for the fueling (59%) at $t = 2.2$ s, while recombination and the main chamber recycling take over more than 50% of the total flux at $t = 4.18$ s, $(\Phi'_{recomb} + \Phi'_{lim} + \Phi'_{IHS})/|\Phi'_{ion}| = 53\%$. This shows that both main chamber recycling and recombination can become important for the fueling of the plasma in AUG.

Assuming that the transport is the same in discharge #36 283, which had similar external discharge parameters, but a larger main chamber wall clearance, it is not surprising that the density was much smaller due to the reduced fueling from the limiters.

### 3.8. Iteration scheme & convergence

In order to guarantee the reproducibility of these results by other EMC3-EIRENE uses some technical details shall be given: The simulation results presented here are obtained by a typical iteration scheme, executing sequences of the routines 'NEUTRAL', 'STREAMING', 'ENERGY' and 'IMPURITY'. As the names suggest 'NEUTRAL' and 'ENERGY', solve the kinetic neutral and the plasma energy transport,

respectively. 'STREAMING' solves continuity and momen-[4] transport simultaneously while 'IMPURITY' has implemented a simplified impurity transport model solving essentially their force balance equation. Rather than running the code with a large number of Monte Carlo particles, here we focus on a large number of iterations, that is of the order of 500 ($\sim$4 days on 32 CPUs) before reaching a 'converged' state. At that point different tracked quantities, like target temperature and the power and particle fluxes, change by less than 2% over the last 30 iterations. The relaxation factor was set to 0.25 for the 'IMPURITY' routine and to 0.5 for the others. Interestingly a slower convergence undergoing rather large oscillations of the mentioned quantities was observed iterating the simulation of an intermediate time point $t = 3.3$ s (not shown here). In L-mode experiments [43] an oscillating phase was observed, when passing from the attached to the detached divertor regime. So possibly the oscillations in the simulation for $t = 3.3$ s have a physical origin.

### 3.9. 2D profiles

Figure 10 shows a poloidal cross-section of the radiation emitted by deuterium and nitrogen $P_{rad,N+D}$ (left) and the ionization distribution (right) for the two simulated time points $t = 2.2$ s (left) and $t = 4.18$ s (right). $P_{rad,N+D}$ is computed according to the data from the ADAS database [44] including the emission from the recombining deuterium. While the strongest radiation and ionization regions are located in front of the targets for $t = 2.2$ s, the radiation and ionization front move towards the X-point at $t = 4.18$ s indicating indeed a detachment of the plasma from the target. In the upper plots (a and b) the lines of sight (LOS) of two bolometry cameras FVC and FHC are also shown. Their measured intensity are color coded by the same color scheme as $P_{rad,N+D}$ but with 1 MW m$^{-2}$ as the maximum. Those LOS that cross regions of large radiation indeed show a large signal confirming a qualitative agreement between the experiment and the simulation. A more quantitative analysis is shown in figure 9, where the simulation data is integrated along these lines (taking into account the actual size of detector and pinhole) and compared to the individual bolometry channels $P_{los}$. First of all the absolute intensity is well reproduced, but this is not too surprising, since the total radiation emitted from nitrogen is controlled during the simulation and an input rather than an output. The upward movement of the maximum radiation from FVC 27 at $t = 2.20$ s to FVC 25 at $t = 4.18$ s is also observed qualitatively in the simulation although the maxima are found for FVC 28 at $t = 2.2$ s and FVC 26 at $t = 4.18$ s. The *quantitative* difference is an indication for the presence of both higher Z (e.g. argon from previous experiments) and lower Z (e.g. boron from the limiter, or helium) radiators. A more refined impurity transport analysis remains as future work.

## 4. Summary

As a preparation for the future upper divertor of AUG a series of small-ELM high triangularity H-mode discharges in upper single-null (USN) was carried out and characterized experimentally. The open divertor geometry allows a large spatial coverage by a single IR thermography camera including both divertors and far-SOL regions extending up to $R - R_{sep} = 100$ mm upstream. Although the distance between the ICRH limiters and the separatrix in the discharge #35 921 is more than ten times the typical near-SOL power fall-off length substantial amounts of power are deposited on these limiters. An explanation for this observation is a substantially higher time averaged far-SOL power fall-off length, that is indeed seen by IR thermography and likely caused by the small ELMs and/or filamentary transport. The time and ELM-averaged power deposition pattern at the outer upper target is well described by the sum of two standard power deposition profiles with the same (time averaged) $\bar{S}$ parameter but different power fall-off length $\bar{\lambda}_q^{near} = 3.8$ mm and $\bar{\lambda}_q^{far} = 25.0$ mm. The far-SOL component contains a substantial fraction of the power and should be taken into account in power exhaust scalings for such a small ELM regime.

The reference discharge #36 283 with very similar external parameters, but a substantially larger clearance to the limiter, showed a lower line-averaged density and larger ELMs, indicating that the limiters have an effect on the discharge itself, e.g. via the recycling of neutral particles or the power loss there, although the causality is not yet identified.

In order to interpret the experimental results EMC3-EIRENE simulations of discharge #35 921 were carried out that now include the main chamber plasma-wall interaction as well as volumetric recombination, recently implemented by the colleagues from the University of Wisconsin. The radial profiles for the time averaged anomalous transport coefficients were adapted according to the upstream density and temperature profiles measured by the He-beam, Thomson scattering, electron cyclotron emission and charge exchange recombination spectroscopy, as well as the target the ion saturation current $j_{sat}$, electron temperature $T_e$ and power deposition $q_\perp$ profiles measured by the divertor Langmuir probes and thermography. A match within the error bars was achieved. Although drifts are not included in EMC3-EIRENE the in/out asymmetry of $q_\perp$ at $t = 2.2$ s is also well reproduced by the code. Partially the asymmetry is explained by the difference in flux expansion and radius $f_{x,IT}R_{OT}/\left(f_{x,OT}R_{IT}\right) = 8.1 \cdot 1.54$ m$/\left(2.8 \cdot 1.26$ m$\right) = 2.4$ at the inner- and outer target, but another substantial contribution is attributed to dissipative processes in the plasma volume at the inner target , that reached detachment, as seen by the up-to downstream pressure drop and simulated electron temperatures below 1 eV. While no $T_e$ measurements are available at the inner target a collapse of $T_e$ is also observed at the outer target in the simulation and by the divertor Langmuir probes at $t = 4.18$ s indicating that both targets are now detached. At that time point the radiative fraction has increased to about 75% and the density at the last closed flux surface by 20% to $2.5 \times 10^{19}$ m$^{-3}$. In addition to that the upstream density shows a rather flat profile (i.e. a 'shoulder') compared to $t = 2.2$ s. The ICRH limiters now receive more power than the outer target and become an important source for particle fueling (in this discharge without
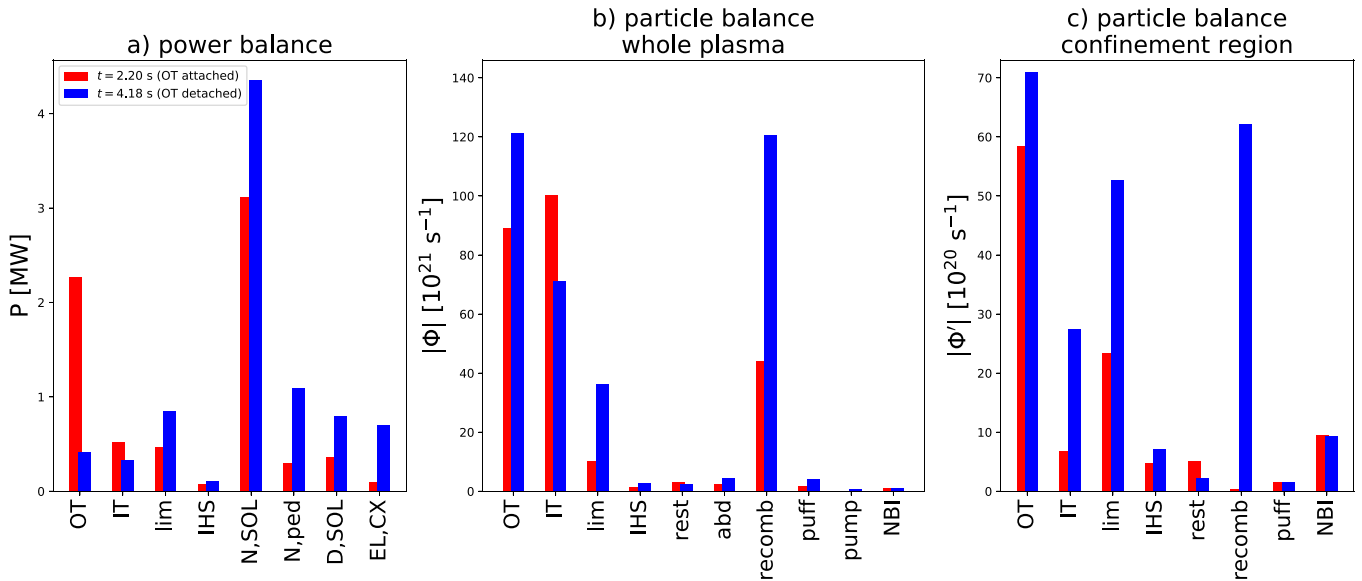
**Figure 9.** Graphical representation of the power- and particle balances. The meaning of the quantities is described in Secs. 3.5–3.7 and the actual values and the signs in table 1. Note the difference of a factor of 20 for the scales in (b) and (c).
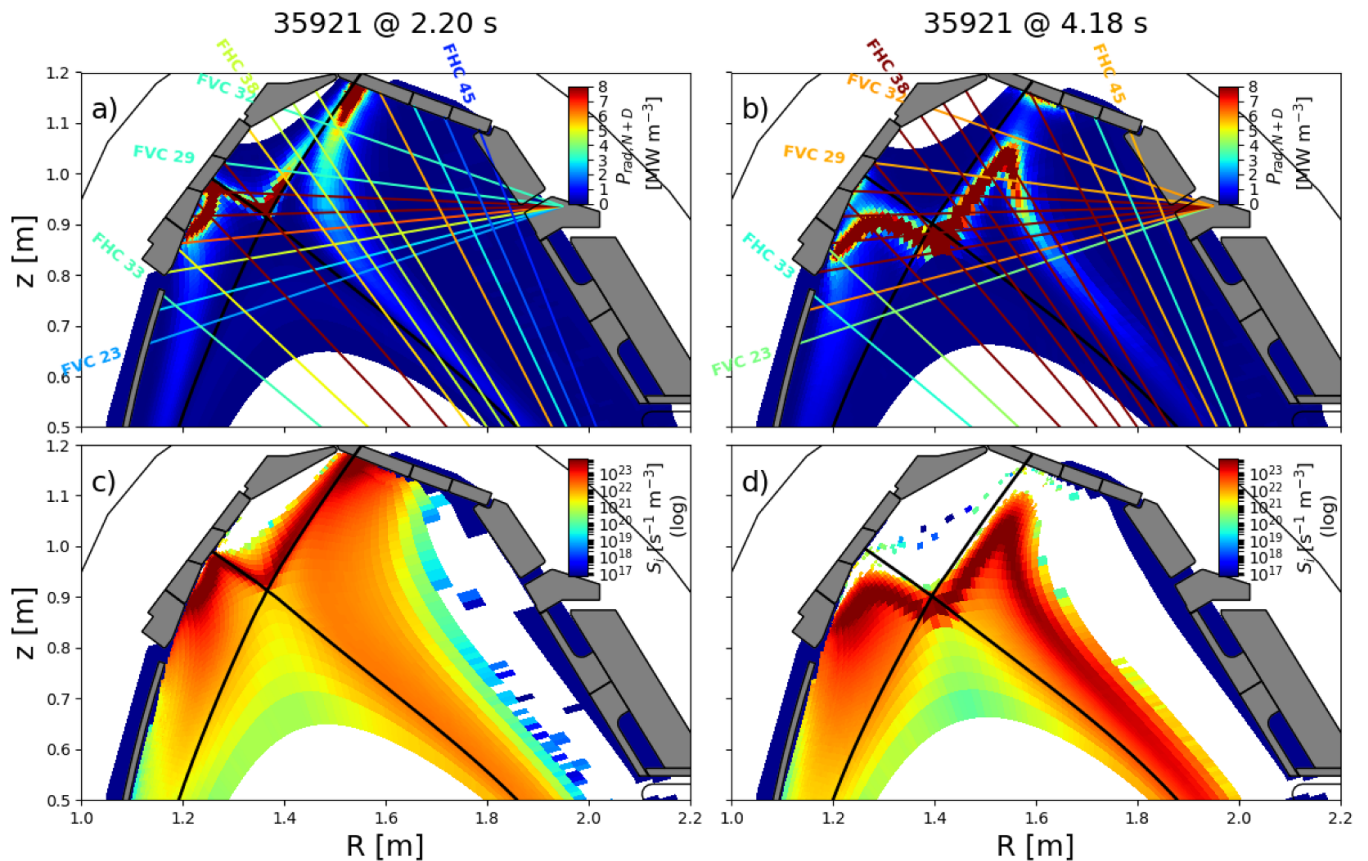


**Figure 10.** 2D plots of the emitted radiation a) and b) and of ionization c) and d). a) and c) correspond to $t = 2.20$ s and b) and d) to $t = 4.18$ s of discharge #35 921. A comparison with line-integrated power measurements from bolometry is shown in figure 11. A detailed description of this figure can be found in section 3.9.

pellets). In order to achieve this agreement with the experiment the time averaged transport coefficients in the simulation were increased for the separatrix near region, although the difference is far less than for those in reference [30]. It seems that at least part of the mechanism responsible for the shoulder formation can be attributed to the reduction of the parallel transport at the low temperatures in the divertor, i.e. to physics that is contained in EMC3-EIRENE.
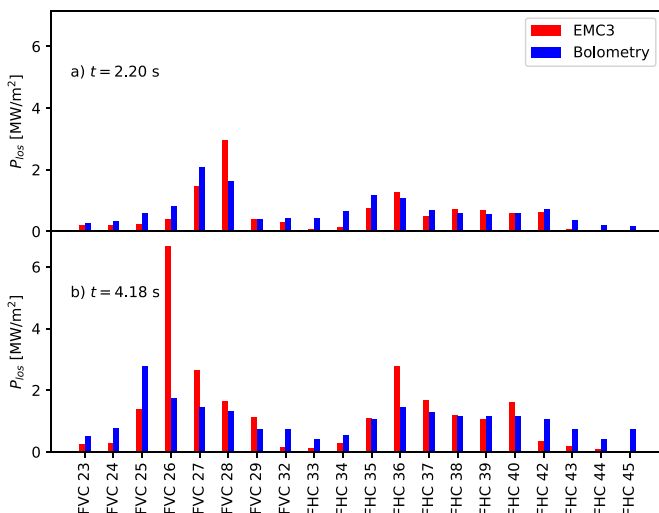
**Figure 11.** Measured (blue) vs. simulated (red) line-integrated power for the time points $t = 2.20$ s (a) and $t = 4.18$ s (b) of discharge #35 921. 2D plots of the emitted radiation are shown in figure 10. More details can be found in section 3.9.

In conclusion we have successfully tested EMC3-EIRENE against experimental data from the edge of an ASDEX Upgrade H-mode discharge with small ELMs before and during detachment of the open upper divertor. It was found that both recombination and main-chamber plasma-wall interaction play an important role and need to be taken into account in general.

## 5. Outlook

After this test of EMC3-EIRENE by detached AUG discharges the obvious next step is to simulate alternative divertor configurations, repeating the study presented in [19] with the new code version, the same external parameters and transport coefficients as well as the recent most planing state of the divertor geometry. A very important physical question is, whether the small but unavoidable error fields provoke strong toroidal asymmetries in the power deposition profile during the detachment or if they will be smeared out by transport. This question needs to be addressed by a 3D code.

## Acknowledgments

## ORCID iDs

T Lunt https://orcid.org/0000-0002-7386-1456
D Brida https://orcid.org/0000-0002-8647-7058
D Carralero https://orcid.org/0000-0002-7824-3307
M Faitsch https://orcid.org/0000-0002-9809-7490
M Griener https://orcid.org/0000-0003-2953-536X
O Pan https://orcid.org/0000-0003-3827-0674
D Silvagni https://orcid.org/0000-0003-2103-3592
M Willensdorfer https://orcid.org/0000-0002-1080-4200

## References

[1] Meyer H *et al* 2019 *Nucl. Fusion* **59** 112014
[2] Eich T *et al* 2011 *Phys. Rev. Lett.* **107** 215001
[3] Eich T *et al* 2013 *Nucl. Fus.* **53** 093031
[4] Kallenbach A *et al* 2015 *Nucl. Fus.* **55** 053026
[5] Asakura N *et al* 1997 *J. Nucl. Mater.* **241–63** 559–63
[6] Carralero D *et al* 2014 *Phys. Rev. Lett.* **115** 215002
[7] Carralero D *et al* 2018 *Nucl. Fus.* **58** 096015
[8] Soukhanovskii V A 2017 *Plasma Phys. Control. Fusion* **59** 064005
[9] Herrmann A *et al* 2019 *Fus. Eng. Des.* **146** 920–3
[10] Lunt T *et al* 2017 *Nucl. Mat. Energy* **12** 1037–42
[11] Pan O *et al* 2018 *Plasma Phys. Control. Fusion* **60** 085005
[12] Lunt T *et al* 2019 *Nucl. Mat. and Energy* **19** 107–12
[13] Loarte A *et al* 2014 *Nucl. Fusion* **54** 033007
[14] Eich T *et al* 2017 *Nucl. Mat. Energy* **12** 84–90
[15] Suttrop W *et al* 2018 *Nucl. Fusion* **58** 096031
[16] Rapp J *et al* 2012 *Nucl. Fus.* **52** 122002
[17] Harrer G *et al* 2018 *Nucl. Fus.* **58** 112001
[18] Mc Carthy P J 1999 *Phys. of Plasmas* **6** 3554–60
[19] Lunt T *et al* 2019 *46th Conf. on Plasma Phys. Milan, Italy, July 8 – July 12, O2.101* (http://ocs.ciemat.es/EPS2019PAP/pdf/O2.101.pdf)
[20] Fischer R *et al* 2016 *Fus. Sci. Tech.* **69** 526–36
[21] Faitsch M *et al* 2015 *Plasma Phys. Control. Fusion* **57** 075005
[22] Nille D, von Toussaint U, Sieglin B and Faitsch M 2018 Probabilistic inference of surface heat flux densities from infrared thermography ed A Polpo, J Stern, F Louzada, R Izbicki and Takada R *Bayesian Inference and Maximum Entropy Methods in Science and Engineering. Maxent 2017* (Cham: Springer) vol 239
[23] Herrmann A *et al* 1995 *Plasma Phys. Control. Fusion* **37** 17
[24] Feng Y *et al* 2004 *Contrib. Plasma Phys.* **44** 1–3, 57–69
[25] Feng Y *et al* 2014 *Contrib. Plasma Phys.* **54** 4–6, 426–431
[26] Reiter D *et al* 2005 *Fus. Sci. Tec.* **47** 172–86
[27] Reimold F *et al* 2017 *Nucl. Mater. Energ.* **12** 193–9
[28] Feng Y 2018 Recent progress in implementing ExB drift in EMC3-Eirene *Poster presented at 23rd International Conference on Plasma Surface Interactions in Controlled Fusion Devices (PSI 23), Princeton, NJ* (http://hdl.handle.net/21.11116/0000-0001-6F90-0)
[29] Feng Y *et al* 2017 *Plasma Phys. Control. Fusion* **59** 034006
[30] Lunt T *el al.* 2015 *J. Nucl. Mater.* **463** 744–7
[31] Asakura N *et al* 2003 *J. Nucl. Mater.* **313–316** 820–7
[32] Kočan M *et al* 2010 *Plasma Phys. Control. Fusion* **52** 045010
[33] Naulin V 2007 *J. Nucl. Mater.* **363–365** 24–31
[34] Coster D P *et al* 2009 *J. Nucl. Mater.* **390–391** 826–9
[35] Griener M *et al* 2018 *Rev. Sci. Inst.* **89** 10D102
[36] Muñoz-Burgos J *et al* 2019 *Phys. of Plasmas* **26** 063301
[37] Brida D *et al* 2017 *Nucl. Fus.* **57** 116006
[38] Paradela Pérez I *et al* 2020 *Contrib. Plasma Phys.* **60** e201900166
[39] Potzel S *et al* 2015 *J. Nucl. Mater.* **463** 541–5

[40] Drenik A 2019 *private communication*
[41] Herrmann A *et al* 2004 *Plasma Phys. Control. Fusion* **46** 971–79
[42] Rohde V 2009 *el al. Plasma Phys. Control. Fusion* **51** 124033

[43] Potzel S *et al* 2014 *Nucl. Fusion* **54** 013001
[44] Summers H P 1994 *Atomic Data and Analysis Structure Users Manual JET-IR 06* (Abingdon: JET Joint Undertaking) https://phys.strath.ac.uk/adas/manual.php